JOURNAL OF GEOPHYSICAL RESEARCH, VOL. 104, NO. D24, PAGES 31,763–31,779, DECEMBER 27, 1999

Use of observed ice crystal sizes and shapes to calculate mean-scattering properties and multispectral radiances: CEPEX April 4, 1993, case study

Greg M. McFarquhar, [1] Andrew J. Heymsfield, [1] Andreas Macke, [2] Jean Iaquinta, [3] and Steven M. Aulenbach [1]

Abstract.

During the Central Equatorial Pacific Experiment, ice crystal sizes and shapes were measured in an outflow anvil. A habit (i.e., column, bullet rosette, Koch fractal polycrystal, sphere) was assigned to each particle using a self-organized neural network based on simulations of how the maximum particle dimension and area ratio varied for random orientations of these crystals. Average ice crystal size and shape distributions were calculated for 25 km long segments at six altitudes using measurements from a two-dimensional cloud probe for crystals larger than 90 μm and a parameterization for smaller crystals based on measurements from the Video Ice Particle Sampler (VIPS). Mean-scattering properties were determined by weighting the size and shape dependent single-scattering properties computed with ray-tracing algorithms according to scattering cross-section. Reflectances at 0.664, 0.875, 1.621, and 2.142 μm were then calculated using a Monte Carlo radiative transfer routine. Although these reflectances agree reasonably with those measured by the MODIS airborne simulator (MAS) above the anvil, uncertainties in cloud base and system evolution prevent a determination of whether ray-tracing or anomalous diffraction theory better predict reflectance. The calculated reflectances are as sensitive to the numbers and shapes of crystals smaller than 90 μm as to those of larger crystals. The calculated reflectances were insensitive to the classification scheme (i.e., neural network, discriminator analysis, and previously used classification scheme) for assigning particle shape to observed crystals. However, the reflectances significantly depended on assumed particle shape.

1. Introduction

The relationship between ice cloud radiative properties and crystal size and shape has not been well quantified. The nonsphericity of ice crystals and the wide variety of crystal shapes prohibit the use of a single theory, such as Mie theory for liquid cloud droplets, to describe the single-scattering properties of ice crystals. Several studies [e.g., *Kinne and Liou,* 1989] have indicated that the radiative properties of clouds can depend significantly on the assumed particle shape.

The single-scattering properties of different idealized ice crystals, including hexagonal cylinders [e.g., *Takano and Jayaweera,* 1995], bullet rosettes [e.g., *Iaquinta et al.,* 1995], complex-shaped Koch fractal polycrystals [e.g., *Macke et al.,* 1996], and randomly deformed spheres [e.g., *Muinonen et al.,* 1996] have been simulated. However, the relationship of the idealized crystal shapes used in studies to actual observed ice crystal shapes has not been well established. A lack of information on the numbers and shapes of ice crystals smaller than 50 μm [*Kinne et al.,* 1992] and on relative numbers of different shapes of ice crystals has also been lacking in previous studies that attempted to compare observed and simulated reflectances.

In this study, a Monte Carlo radiative transfer program (developed by A. Macke, 1994) is used to simulate fluxes and radiance fields using observed size distributions obtained with instrumentation on the Aeromet Lear jet in a blow-off anvil on April 4, 1993, during the Central Equatorial Pacific Experiment [*McFarquhar and Heymsfield,* 1996]. The simulated reflectances are compared to multispectral reflectances measured by the MAS, mounted on the ER-2, which flew in synchronization with the Lear jet at 19 km height above the ground. The weaknesses of past studies are some-

[1]National Center for Atmospheric Research, Boulder, Colorado.

[2]Institut fuer Meereskunde, Universität zu Kiel, Cologne, Germany.

[3]Ussel, France.

Paper number 1999JD900802.
0148-0227/99/1999JD900802$09.00

what ameliorated by using two-dimensional images of ice crystals as small as 5 μm obtained with a Video Ice Particle Sampler (VIPS) [*Heymsfield and McFarquhar,* 1996] together with images of larger crystals from a two-dimensional cloud (2-DC) probe [*McFarquhar and Heymsfield,* 1996] (hereinafter referred to as MH96) to define the size and shape distributions needed for calculating the mean-scattering properties at each location in the cloud. The single-scattering and polarization properties for the different idealized ice crystals, upon which the mean-scattering properties are based, are calculated using geometric optics and the far-field diffraction approximation [*Macke,* 1993; *Macke et al.,* 1996].

Because of uncertainties in the location of cloud base and the temporal evolution of the system, an evaluation of the strengths and weaknesses of different radiative transfer codes is complicated; only a general comparison is possible. The measured reflectances are additionally used to guide the choice of cloud base for the simulated cloud. However, sensitivity studies yield information about the role of different crystal sizes and shapes in determining cloud radiance. The applications of the findings to remote sensing and climate studies are discussed.

2. Single-Scattering Properties of Randomly Oriented Crystals

For this study, observed ice crystals are assigned one of the following shapes: sphere, column, bullet rosette, or polycrystal. The detailed morphometric information about these particle shapes (i.e., aspect ratios, pyramid angles, deformation parameters) replicates measured ice crystals as closely as possible.

The relationship between diameter and length for hexagonal columns was assumed to follow *Heymsfield's* [1973] relationship derived from microphotographs of replicas of ice crystals collected in silicone oil. This relationship differs only slightly from those of *Auer and Veal* [1970] and *Mitchell and Arnott* [1994] but differs more substantially from the relationship originally used to process the CEPEX data [e.g., MH96]. For the purpose of this study, particles with lengths greater than 1000 μm were never classified as columns because such large columns were not observed during CEPEX. Contrary to the study of *Macke et al.* [1998], where columns were randomly oriented in three dimensions, here the hexagonal columns were assumed to fall with their long axis oriented horizontally, which is true for Reynolds numbers up to approximately 150. The crystals were randomly oriented in the horizontal. Any wobbling of the falling hexagonal crystals has been estimated as ±6% [see *Jayaweera and Mason,* 1965] and hence is ignored. *Macke et al.* [1996] showed that light scattering from hollow columns is representative of the scattering from most column-like particles, including hollow columns, solid bullets, and hollow bullets. Hence there was no need to distinguish between such forms in this study.

An assemblage of six branches, each oriented along one of the three-dimensional base vectors (i.e., x, y, z, -x, -y, and -z), was used to describe the bullet rosette geometry [*Iaquinta et al.,* 1995, Figure 2, crystal 6-3] and calculate the single-scattering properties. The aspect ratio of each branch was identical to that of a column with the same length. Six branches was chosen as an average number based on observations from previous campaigns; estimates on the number of arms has ranged from 3-5 [*Krupp,* 1991; *Miloshevich et al.,* 1992] to as many as 11 [*Arnott et al.,* 1994]. Measures that aid in habit identification, such as area ratio and perimeter ratio, did depend on the number of branches, but *Iaquinta et al.* [1995] found that although the lateral and backward scattering from a rosette increased with the number of bullets, the normalized scattering phase functions differed by only 20% for crystals with three-dimensional random orientations. Hence provided that the habit identification is performed correctly, differences due to the number of branches should not affect the single-scattering properties significantly. The angle of the pyramid making up the tip of the columns is estimated as 60° [*Heymsfield,* 1972]. The bullet rosettes are randomly oriented in three dimensions as they fall.

Macke et al. [1996] approximated the difficult and highly complex geometric structure of a polycrystal by means of a three-dimensional Koch fractal, finding that a second generation polycrystal provided a similar scattering behavior to a third generation polycrystal. *Macke et al.* [1996] also found that increasing the distortion of the polycrystals did not significantly alter the asymmetry parameter, and changes in radiance fields due to increasing the distortion of the Koch fractal are rather small [A. Macke, personal communication, 1998]. Hence undistored randomly oriented second-order polycrystals are used in the experiments reported here.

The single-scattering properties of these idealized crystals were computed at the MAS solar and near-infrared wavelengths (0.664, 0.875, 1.621, and 2.142 μm). The real and imaginary indices of refraction, shown in Table 1, were computed for these channels using the MAS spectral response functions and tabulated optical constants [*Warren,* 1984; *Kou et al.,* 1994; *Perovich and Govoni,* 1994]. The properties were computed over a much wider range of crystal sizes than used by *Macke et al.* [1998] in order to take into account the high reso-

Table 1. Real and Imaginary Indices of Refraction Used for Computing Radiative Properties of Ice Crystals

λ	$\Delta\lambda$ (μm)	n_i	n_r
0.664	0.055	1.30781	1.67508e-8
0.875	0.041	1.30364	2.85923e-7
1.621	0.057	1.28863	2.51486e-4
2.142	0.047	1.26596	4.30201e-4

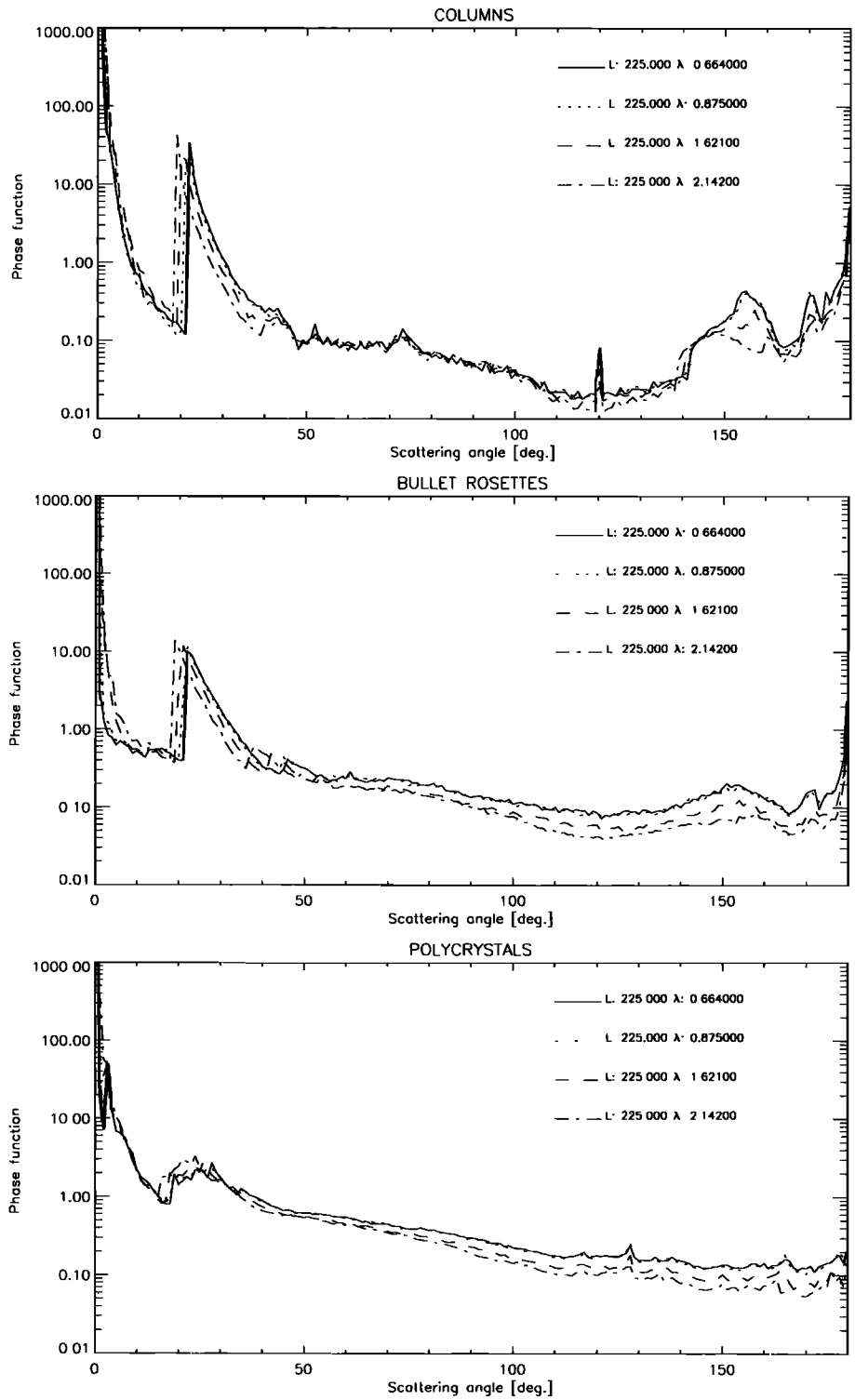

Figure 1. Normalized phase function calculated using Macke ray-tracing code for two-dimensional randomized orientations (columns, top) and three-dimensional randomized orientations (bullet rosettes, middle; polycrystals, bottom) of 225 μm crystals at solar and near-infrared wavelengths.

lution and shape information available from the in situ probes. Thirty-seven different crystal sizes were used to compute the single-scattering properties, varying from 5 μm to 2.7 mm, reflecting the sizes of the observed crystals. The corresponding size parameters ($x = 2\,\frac{\pi r}{\lambda}$) range from 23.7 to 12774 for $\lambda = 0.664$ μm and from 7.4 to 3960 for $\lambda = 2.142$ μm.

The single-scattering properties (i.e., mean-scattering

phase matrix $P_{i,j}(\theta)$, mean single-scattering albedo ω_0, and mean asymmetry parameter g) were then computed using a routine [developed by A. Macke, 1996] which calculates the reflection and transmission processes of a bundle of parallel and equidistant incoming rays to the particle. Additionally, the diffraction at the crystal's geometrical cross section was computed for each of the random orientations of the crystal using the far-field approximation. The model phase functions were computed for 0.25°, 179.75°, and every degree between 1° and 179°. The size parameters are greater than 30 for all but the smallest bin size, which does not contribute substantially to the extinction and has its base scattering properties computed by Mie theory (section 3); hence the use of ray tracing for calculating the scattering properties is justified. For each crystal, 10,000 random orientations with 100 rays per crystal orientation were used to compute the single-scattering properties. These numbers offer a reasonable compromise between calculation speed and accuracy of simulated properties.

Figure 1 shows examples of the phase functions for different wavelengths and different crystal shapes. For columns, despite differences in aspect ratio from those used by *Macke et al.* [1996, 1998], the phase functions appear similar to theirs with the 22° and 46° halo maxima. The bullet rosette, with its component bullets, clearly exhibits the 22° peak but not the 46° peak because of multiple total internal reflections and because of the pyramidal top which disables transmission at 90° prisms.

3. Application of Idealized Shapes to Observed Crystals

The crystal shapes for which the single-scattering properties are calculated are idealized representations of the shapes that occur in natural cirrus. Several examples of in situ measured crystals in outflow anvils during CEPEX are presented by MH96 and *Heymsfield and McFarquhar* [1996]. Very few of them are exact replicas of the idealized crystals used in this study as the observed shapes are highly variable, irregular, and nonuniform, making it difficult to characterize them by idealized crystals. This is especially true for the polycrystals, which do not truly have the Koch-fractal shape; in reality, polycrystals can include spatial crystals, aggregates, other irregular crystals, and potentially bullet rosettes. Nevertheless, the idealized crystals were chosen to offer the best possible representation of the observed crystals.

The observed in situ size distributions are represented as functions of crystal maximum dimension (which for the remainder of this paper is the maximum dimension either parallel or perpendicular to the flight direction because this is the quantity measured by the in situ probes) and area ratio (which is the ratio of the measured cross-sectional area compared to that of a circumscribed circle). A habit, or idealized shape, is assigned

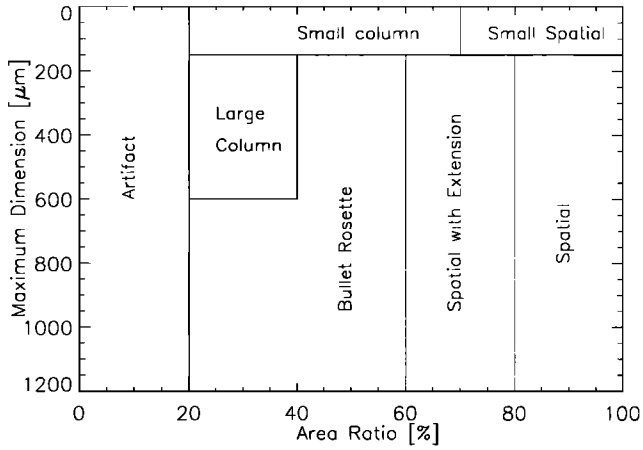

Figure 2. Habit classification scheme originally used to process Central Equatorial Pacific Experiment data. A habit is assigned to each crystal depending on the measured maximum dimension and area ratio.

to each particle based on these two measured quantities. Figure 2 shows the habit classification scheme that was originally used to process the CEPEX data from the April 4, 1993, case study.

To better relate the observed crystals to the idealized crystals, a refined habit classification was also implemented. Simulations of one thousand random orientations of each of the idealized crystals were performed in order to determine the maximum dimensions and area ratios that would be measured by a VIPS or 2-DC probe. The mass and volume of the crystals were invariant under these orientations. Using these results, two different techniques were then applied to assign a crystal habit to each particle given the maximum dimension and area ratio.

The first technique used a discriminate analysis. Inspection of the simulation results shows that for a given crystal maximum dimension, columns, bullet rosettes, and polycrystals have increasing area ratios. Hence for a given maximum dimension the maximum likelihood area ratio that divides the populations of columns/bullet rosettes, and bullet rosettes/polycrystals is calculated. The classification success rate is defined as the fraction of crystals with a known shape that would be identified as having that shape from the simulation results when the discriminant analysis classification scheme is applied. The success rate for the discriminate analysis was 76% for columns, 31% for bullet rosettes, and 90% for polycrystals. Given the complexities of naturally occurring ice crystals, it is likely that the rate of successful identification of their shapes would be lower. It was also found that this method for assigning particle habit does not work well when all three habit types occur simultaneously.

Therefore a second technique, a self-organized neural network [*Kohonen*, 1995] was implemented to assign habit. The outputs of the network are poles (or

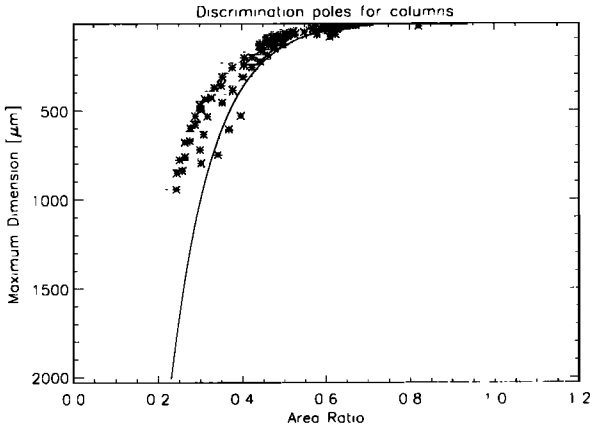

Figure 3. Simulated maximum dimension and area ratio for various sizes of hexagonal columns with preferred orientation of fall (dots). Asteriks represent discrimination poles or attractive vectors used in neural network classification scheme. Solid line represents area ratio, as a function of maximum dimension, which divides columns from bullet rosettes based on a discriminator analysis.

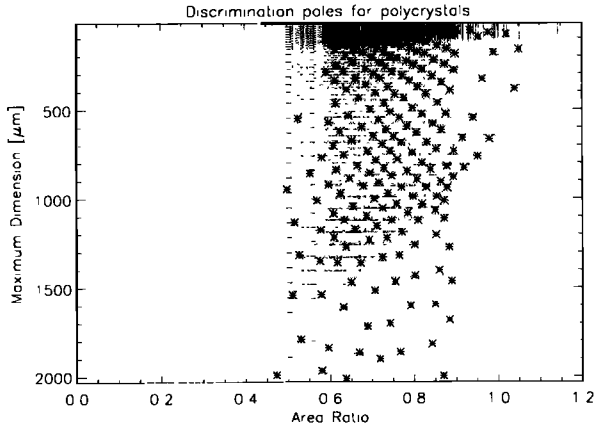

Figure 5. Same as Figure 3 except dots and asteriks represent simulations and discrimination poles for random orientations of various sizes of polycrystals.

attractive vectors) in the two-dimensional maximum dimension–area ratio space. The habit of an observed crystal is defined as the habit of that pole with the smallest Cartesian distance from a point (i.e., maximum dimension, area ratio pair) in the two-dimensional space. Figures 3, 4, and 5 show that the poles define zones where the habit is likely to be a column, bullet rosette, or polycrystal. The dots represent the maximum dimensions and area ratios that are determined from the results of the random crystal orientations. Although the zones appear to follow the dividing lines separating columns from bullet rosettes (Figure 3), the success rate of the classification scheme is much better: 85% for columns, 69% for bullet rosettes, and 87% for polycrystals. Various sets of poles were tried, and the illustrated set of poles reached a compromise between the number of poles and the accuracy of the classification scheme. This scheme was used to define ice crystal habit for the base simulation described in section 4.

The maximum dimension of a crystal is related but not equal to the length of the crystal (e.g., length of column, length of bullet in a bullet rosette, or principal dimension of the polycrystal). To relate the observed crystal maximum dimensions, either parallel or perpendicular to the flight direction, to the lengths of the idealized crystals, the relationship between them was parameterized using the simulation results. Figure 6 shows an example of this relationship for bullet rosettes. The relationships are given by

$$L_c = \max(-6.84 + 1.079D, D),\ r = 0.996224; \quad (1)$$

$$L_c = \max(-7.24 + 0.537D, 0.5D),\ r = 0.992203; \quad (2)$$

$$L_c = \min(14.64 + 0.927D, D),\ r = 0.987027; \quad (3)$$

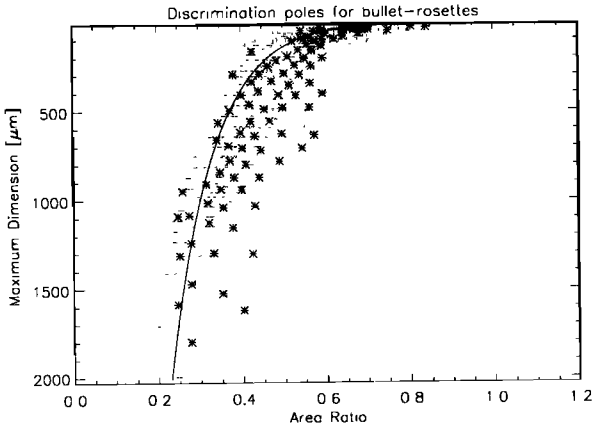

Figure 4. Same as Figure 3 except dots and asteriks represent simulations and discrimination poles for random orientations of various sizes of bullet rosettes.

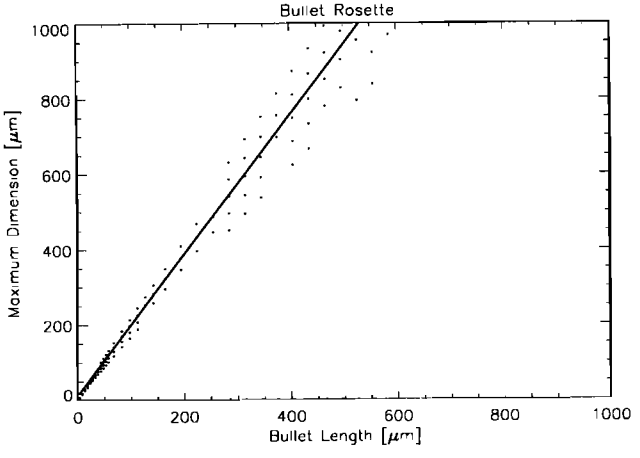

Figure 6. Relationship between bullet length and maximum dimension that would be observed by an optical array probe. Dots represent data points obtained from three-dimensional random orientations of bullet rosettes; solid line represents best fit to the data.

Table 2. D_{ge} and β_{ext} (in Parenthesis) for Six Different Grid Boxes and Six Altitudes Determined From Average Size Distributions and *McFarquhar and Heymsfield,* [1997], Parameterization of Small Crystal Contributions

Alt. [km]	178.0 - 178.25	178.25 - 178.5	178.5 - 178.75	178.75 - 179.0	179.0 - 179.25	179.25 - 179.5
13.2	5.5 (0.0002)	—	13.6 (0.08)	7.3 (0.005)	23.8 (0.44)	16.3 (0.14)
12.4	24.6 (0.62)	8.5 (0.02)	28.8 (0.97)	26.8 (0.76)	20.5 (0.32)	23.3 (0.45)
12.0	13.9 (0.08)	24.2 (0.48)	29.0 (0.78)	28.2 (0.70)	31.0 (0.89)	26.0 (0.50)
11.4	23.2 (0.4)	28.2 (0.76)	31.8 (1.1)	30.0 (0.94)	31.2 (0.86)	25.2 (0.51)
10.9	31.7 (2.2)	31.1 (2.2)	31.5 (2.3)	35.4 (3.3)	28.1 (1.5)	26.9 (1.3)
9.9	34.3 (7.4)	38.1 (12.3)	38.5 (11.9)	41.4 (16.9)	43.0 (17.6)	35.3 (9.9)

where D is the maximum dimension of the ice crystal in the x or y direction, and L_c, L_{br}, and L_p are the length of a column, a branch on a bullet rosette, and the base of the tetrahedron for the polycrystal, respectively. The regression coefficients suggest that the fits are reasonable and that there is no need to add another variable, such as area ratio, to characterize these relationships.

During CEPEX, a dedicated microphysics/radiation mission was flown on April 4, 1993, where the properties of an anvil produced from deep convection were sampled at several different altitudes (either parallel to or directly against the outflow direction) by a Lear jet equipped with microphysical instrumentation. In addition, an ER-2 equipped with remote sensors and radiometers flew directly above the Lear jet at an altitude of 19 km. The MAS, developed for providing multispectral images of outgoing radiation for developing and validating remote sensing algorithms, measured solar and infrared radiation in 12 narrowband channels between 0.66 and 13.95 μm. The spectrometer scans a swath width of 37 km (85.92°) perpendicular to the flight track, producing images with a spatial resolution of 50 m at nadir [*King et al.,* 1996]; only the nadir data were used in this study. The solar zenith angles during the measurement periods ranged from 20° to 30°, with an average of 23.6°.

To understand the horizontal and vertical structure of the anvil, MH96 divided the approximately 150 km long legs into six different segments. Here the average size and area ratio distributions for each of the six different grid boxes at the six different altitudes from the 2-DC probe are determined. Table 2 gives the extinction coefficient β_{ext} and the generalized effective diameter D_{ge} [*Fu,* 1996], for the six horizontal boxes at the six altitudes at which the Lear jet flew. The upper layers have lower β_{ext} and D_{ge}, showing the importance of small crystals at the top, whereas the lower layers are dominated by greater β_{ext} and D_{ge}. The average reflectance measured by the MAS for each grid box is also determined; since the ER-2 repeated its flight track 6 times, the average reflectance and its standard deviation for each grid box is computed.

The contribution of small crystals is added to these distributions using *McFarquhar and Heymsfield's* [1997] parameterization of the size distribution of small ice crystals. The manner in which this parameterization was applied is slightly different than that described in the original paper. Here only contributions of crystals with maximum dimensions smaller than 90 μm were parameterized; those with a maximum dimension greater than 90 μm were based on the 2-DC measurements. Note also that the contributions of small crystals parameterized by both the first-order gamma and the lognormal in the *McFarquhar and Heymsfield* [1997] parameterization must be included in order to obtain an accurate assessment of the small crystal population. Direct measurements from the VIPS are not utilized because the required analysis would be very time consuming, because the quality of the VIPS images varies substantially and because the VIPS data become saturated whenever the ice water contents (IWCs) are high. Shape information is not available explicitly for the small crystals. *McFarquhar and Heymsfield* [1996] determined that the majority of the two-dimensional images of these smaller crystals were "quasi-circular." Some of the crystals appeared to be remnants of frozen drops, whereas others could only be identified to have rounded edges. No evidence of the irregularities associated with the polycrystal model was seen, and hence the Mie theory of scattering is used to calculate radiative properties for the base study described later. The importance of this assumption is addressed through sensitivity studies.

Figure 7 shows examples of the size and habit distributions of particles that were measured at four altitudes for the longitude range 178.5 to 178.75° during the mission (and at a latitude of approximately 15°S, all locations are quoted only in terms of longitude hereafter; see MH96 for detailed flight track). The different shadings represent the different habits. Polycrystals were the most predominant crystal habit for most time periods on April 4. Of the crystals measured by the 2-DC, 33.7% were classified as columns, 24.7% as bullet rosettes and 41.6% as polycrystals. Small crystals from the parameterization dominated the total concentration, representing approximately 98% of the number. In terms of cross-sectional area, which is most closely related to the extinction at visible wavelengths, small crystals contribute 56% of the total. For the large crystals, 18% of the cross-sectional area was contributed by

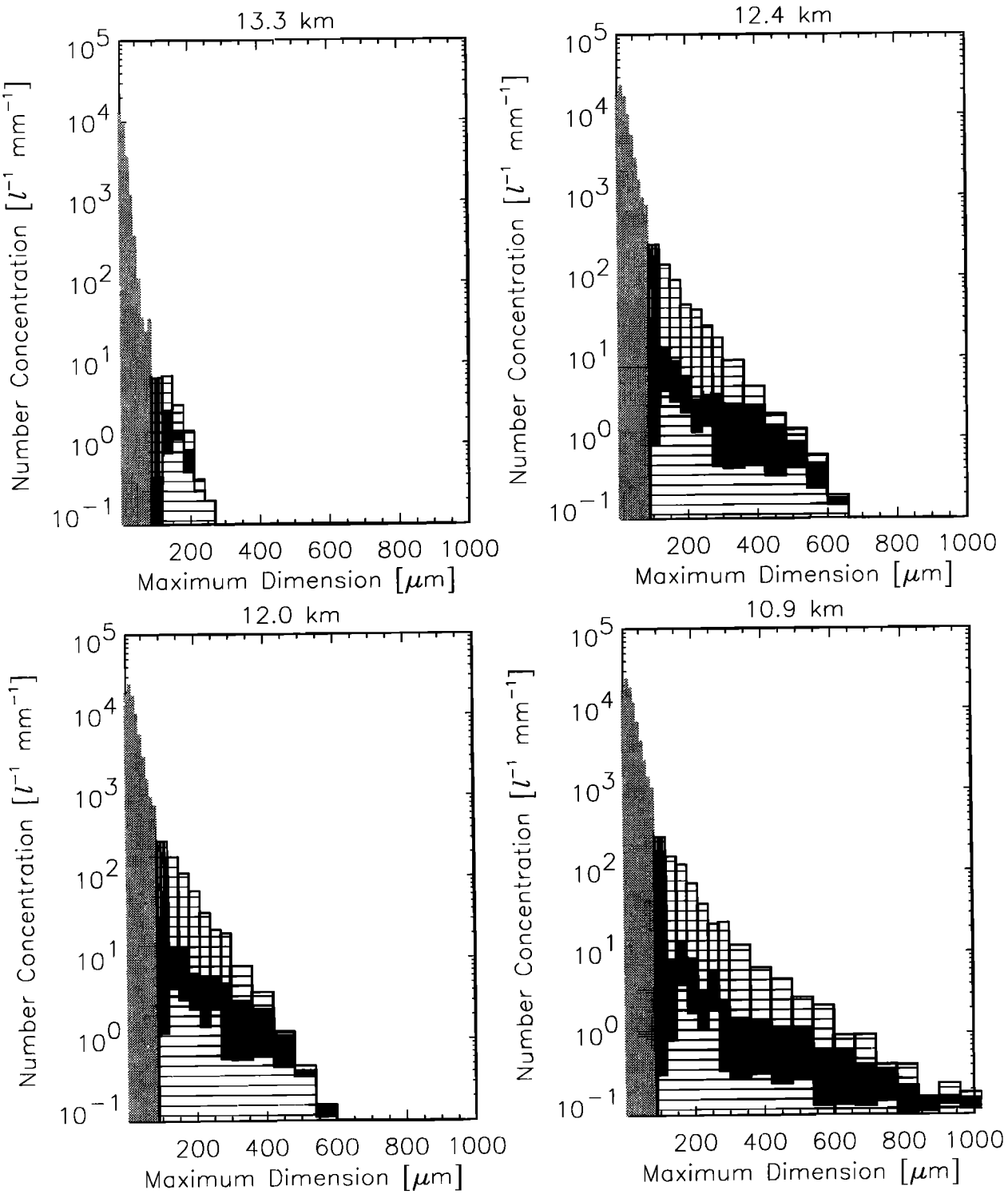

Figure 7. Examples of size and shape distributions at four altitudes, obtained at longitudes between 178.5° and 178.75°. Horizontal axis is maximum dimension observed by optical array probe. Gray shading represents small crystal contributions obtained from MH97 parameterization. Solid lines represents fractional contributions from columns, solid shading, contributions from bullet rosettes, and hatched pattern represents contributions from polycrystals.

columns, 29% by bullet rosettes, and 53% by polycrystals. This shows the importance of obtaining a good representation of both the small crystals and the polycrystals. It should be reemphasized here that the crystals classified as a particular shape do not necessarily have that exact shape; they are classified as such because their shape characteristics are most similar to those shapes. It is therefore expected that their single-scattering characteristics will be most like those idealized crystals.

Table 3. Mean Asymmetry Parameter as Function of Altitude, Obtained From Ray Tracing, for All Grid Boxes During April 4 CEPEX Case Study for Multiple Wavelengths (at 0.664, 0.875, 1.621, and 2.142 μm)

Alt [km]	178.0-178.25	178.25-178.5	178.5-178.75	178.75-179.0	179.0-179.25	179.25-179.5
13.2	.853;.846;.835;.835	—;—;—;—	.869;.866;.864;.864	.858;.853;.847;.847	.862;.861;.868;.874	.867;.865;.866;.868
12.4	.857;.856;.865;.871	.856;.853;.851;.852	.854;.853;.866;.874	.856;.856;.867;.874	.863;.862;.867;.871	.862;.861;.868;.873
12.0	.867;.865;.863;.865	.856;.856;.864;.870	.854;.853;.866;.873	.856;.855;.867;.875	.854;.854;.872;.880	.860;.859;.869;.875
11.4	.862;.861;.867;.872	.857;.856;.868;.875	.853;.853;.868;.876	.853;.853;.869;.876	.856;.856;.872;.880	.860;.860;.870;.876
10.9	.851;.851;.867;.876	.850;.850;.868;.876	.848;.848;.868;.877	.844;.844;.865;.876	.856;.856;.869;.876	.856;.855;.868;.875
9.9	.849;.849;.871;.881	.835;.836;.870;.882	.837;.838;.867;.879	.825;.826;.870;.883	.817;.819;.883;.895	.836;.837;.872;.883

4. Radiative Transfer Calculations

4.1. Calculation of Mean-Scattering Properties

For each longitude and height interval for the April 4, 1993, case study, the single-scattering properties were calculated using the habit-dependent size distributions. Following *Macke et al.* [1998], the mean single-scattering properties for the distribution of particles were calculated as

$$< X > = \frac{\sum_k \sum_L \sum_a X_k(L) N_k(L,a) C(L,a)}{\sum_k \sum_L \sum_a N_k(L,a) C(L,a)}, \quad (4)$$

where $X = P(\theta)$, $\tilde{\omega}_0$, or g, the subscript k represents particle shape, $N_k(L,a)$ is the size distribution of shape k with length L and area ratio a, and $C(L,a)$ is the scattering cross section of the appropriate size particles. The scattering cross sections were computed on the basis of geometric optics and the far-field diffraction approximation [*Macke et al.*, 1998]. The resolution used to compute the mean-scattering properties was much finer than that used by *Macke et al.* [1998]. Whereas *Macke et al.* [1998] used six different maximum dimensions in their study (25, 50, 100, 200, 400, and 800 μm), 37 different maximum dimensions were used in this study, accounting for finer details of the size distributions.

The mean single-scattering properties were computed for each of the grid boxes at the five solar and near-infrared MAS wavelengths. Table 3 and Table 4 give the mean asymmetry and mean single-scattering albedo as a function of altitude for different wavelengths. Their variations with height are principally caused by varying contributions of small and different shaped particles to the total. For example, at higher altitudes, the asymmetry parameters range from 0.85 to 0.87, close to the asymmetry parameters for the spherical particles (ranging from 0.84 to 0.88) and columns (0.79 to 0.85) which dominate at these altitudes. At lower altitudes the visible asymmetry parameters are lower (0.80 to 0.85) due to the increasing contributions from bullet rosettes (asymmetry parameters ranging from 0.77 to 0.84) and polycrystals (asymmetry parameter of 0.74). At near-infrared wavelengths, for example, 2.142 μm, the mean asymmetry parameter increases closer to cloud base because the asymmetry parameters of the larger bullet rosettes (0.91 for crystal with maximum dimension of 700 μm) and polycrystals (0.89 for 700 μm) are larger than those of the smaller spherical particles (0.82 to 0.89) which are more important at higher altitudes. The height variation of the the single-scatter albedo can be explained by the greater fractions of larger particles, which absorb more radiation, at the lower altitudes.

Figure 8 shows examples of the mean-scattering phase function for the four size distributions depicted in Figure 7 for three different solar and near-infrared wavelengths. The vertical arrows indicate the range where

Table 4. Mean Single-Scattering Albedo as Function of Altitude, Obtained From Geometric Optics, for All Grid Boxes During April 4 CEPEX Case Study for Multiple Wavelengths (at 1.621 (2.142) μm)

Alt. [km]	178.0 - 178.25	178.25 - 178.5	178.5 - 178.75	178.75 - 179.0	179.0 - 179.25	179.25 - 179.5
13.2	.984(.980)	---(---)	.972(.965)	.978(.973)	.958(.949)	.967(.960)
12.4	.959(.949)	.975(.969)	.951(.939)	.953(.943)	.963(.954)	.959(.949)
12.0	.971(.964)	.959(.949)	.952(.941)	.952(.940)	.941(.928)	.955(.944)
11.4	.961(.951)	.951(.940)	.947(.935)	.946(.934)	.942(.929)	.954(.943)
10.9	.945(.932)	.943(.930)	.940(.927)	.938(.924)	.949(.937)	.950(.939)
9.9	.933(.920)	.915(.899)	.923(.908)	.899(.882)	.864(.847)	.913(.898)

the scattering phase functions are sampled, given the nadir view and the calculated solar zenith angles. When compared with Figure 1, the most noticeable features are the smooth nature of the phase function and the absence of the 22° and 46° halos. This happens because small-scale features are removed when averaged over the wide range of shapes and sizes making up a size distribution and because there are insufficient numbers of columns or bullet rosettes to make the halos stand out. The peak between 130° and 140°, which is especially prominent for the solar wavelengths and near cloud top, occurs because the size distributions are dominated by smaller particles; the phase function hence tends toward the spherical phase functions predicted by Mie theory. However, this part of the phase function was not sampled at nadir, as indicated by the vertical lines. Previous observations with the tilt scan CCD camera radiometer [e.g., *Spinhirne et al.*, 1996] have indicated characteristic angular functions of visible reflectance for cirrus that are flatter than those predicted by Mie scattering models. Hence spheroids [*Mishchenko et al.*, 1997] could be used for simulating the radiative properties of smaller crystals.

4.2. Comparison with Observations

The phase functions, single-scattering albedos, and extinction optical depths obtained from the average size and shape distributions were used with a Monte Carlo radiative transfer program (developed by A. Macke, 1994) for computing fluxes and radiance fields. The wavelength-dependent surface albedo was based on the lowest recorded reflectances of the MAS over the ocean surface on April 4. Table 5 lists these wavelength-dependent albedos.

Figure 9 illustrates how the calculated reflectances at the top of the atmosphere varied as a function of longitude. The asteriks represent the reflectances calculated using ω_0 and β_{ext} obtained from the ray-tracing code, and the solid circles represent those calculated using ω_0 and β_{ext} obtained from anomalous diffraction theory (ADT) as discussed in section 4.3. The solid line is drawn between the average reflectance measured by the MAS on the ER-2, with the vertical bars representing the standard deviation of the reflectance. The quality of the MAS data is lower than that from most projects on which the MAS recorded data but should be sufficiently high for the sensitivity studies to be reported here. The standard deviations are large because the system began to decay during the mission, and because the movement of the system meant that the same location of the storm was not always sampled at each longitude [see *McFarquhar and Heymsfield*, 1996]. Because of possible smaller-scale circulations [*Lilly*, 1988], complex air trajectories associated with deep convection, and inadequate knowledge of the three-dimensional structure of the anvil, it was not possible to follow different parts of the storm at different times. The calculated visible reflectances tend to be larger toward the eastern portion of the track, as caused by the larger ice water contents and optical depths closer to the remnants of the convection. However, the observed visible reflectances decrease. The observed brightness temperatures, measured by both the MAS and the Geostationary Meteorological Satellite (GMS), were also lower at the eastern edge of the track (figure not shown). Longitudnal trends for the near-infrared reflectances, dominated by the sizes and shapes of cloud particles at the top of the cloud, are not so prominent.

4.3. Sensitivity Studies

Even though it is difficult to compare the observed and simulated reflectances, the April 4, 1993, CEPEX case still offers one of the few horizontal and vertical profiles of microphysical properties that have been obtained within a tropical anvil. Therefore using observed size and shape distributions as a guide, the modeled results are used to determine the most important factors that affect the observed multispectral reflectances. Table 6 summarizes the sensitivity studies that were performed in this investigation. One parameter was varied for each series of sensitivity studies. For the base case, the conditions listed under study 1) for all series were used. For all six series, the mean-scattering phase function β_{ext} and ω_0 were computed independently for each of the experimental runs.

For series 1, in Figure 9 the solid circles represent the reflectances calculated using ω_0 and β_{ext} from ADT,

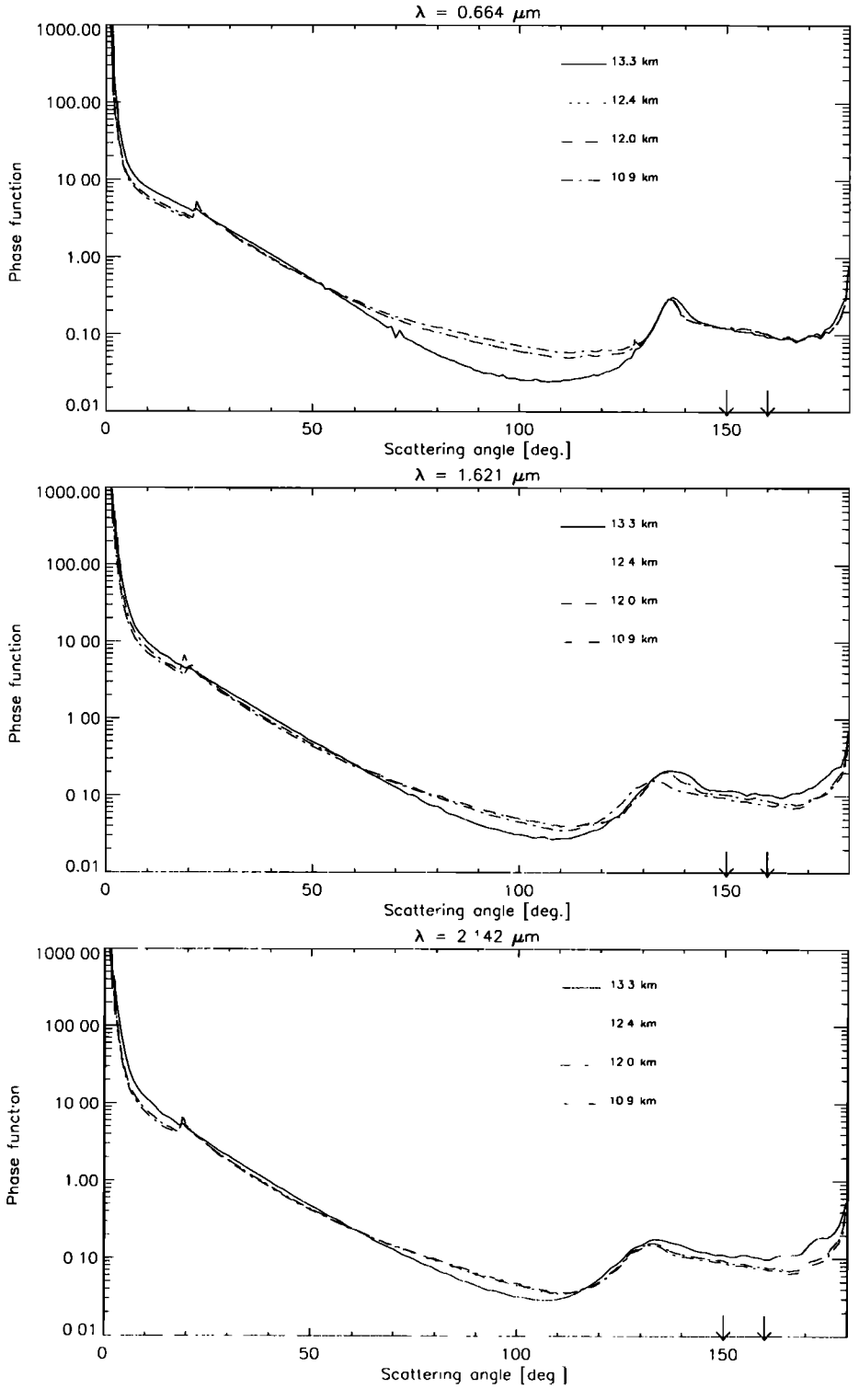

Figure 8. Mean-scattering phase function for 0.664, 1.621, and 2.142 μm for different heights in the cirrus anvil, for average spectra at longitudes between 178.5° and 178.75°. Vertical arrows indicate the range where scattering phase functions are sampled.

using the equations presented by *Mitchell and Arnott* [1994]. The phase functions were computed by normalizing the ray-tracing phase functions by the scattering cross sections computed with ADT since ADT is only appropriate at small scattering angles and ignores reflection and refraction. As stated at the end of section 2, the size parameters are greater than 30 for all but the smallest bin, showing that anomalous diffraction theory results should asymptote to the correct values. The visible reflectances for the two methods are al-

Table 5. Wavelength-Dependent Surface Reflectance Based on MAS-Measured Reflectance Over the Ocean Surface

λ (μm)	Surface Reflectance
0.664	0.057
0.875	0.041
1.621	0.037
2.142	0.014

most identical, as expected, with more differences in the near-infrared channels. However, given the large standard deviations in the observations, it is not possible to evaluate the performance of either radiative transfer scheme with high precision, or to determine which more realistically represents the observed reflectances. The simulated reflectances match the observed reflectances within their error bars. The ray-tracing extinction coefficients from ray tracing are 5.9% larger than those from anomalous diffraction theory on average and exhibit little dependence on the magnitude of the extinction coefficient (figure not shown). No substantial differences in the mean-scattering phase functions, caused by differences in the scattering cross sections, for the two methods were observed.

Series 2 analysis was performed to address the large uncertainty associated with the extinction optical depth τ_{ext} calculated from the microphysical data. This large uncertainty is due to the necessity of using the Lear jet point measurement as the representative value of a height interval within the cloud. More importantly, the cloud base is not well known because of the lack of a radar on either the Lear jet or the ER-2 and the occultation of the ER-2 lidar system before it penetrated the cloud. MH96 noted that the cloud was first detected at 7 km during the ascent of the Lear jet. Lacking additional quantitative data, 7 km is assumed to be cloud base, but this cannot be assumed representative of the entire cloud because the pilots noted that the cloud had a classic anvil upward slope.

For simulation 2a, the base case, the cloud measurements represent a grid box centered at the measurement location, with geometric thicknesses of half the distance to the higher and lower legs. The uppermost penetration, at heights between 13.2 and 13.3 km, was assumed to be 100 m below cloud top. When changing the base and top of the grid boxes that characterize the cloud measurements without adjusting the cloud base (cases e and f), the reflectances did not change substantially. However, reflectance did exhibit a greater sensitivity to the assignment of cloud base (varied between 6 and 9 km to reflect its uncertainty), especially for the 0.664 and 0.875 μm channels. This is shown in Figure 10 where the dotted lines show how the top of the atmosphere reflectance varies depending on the assumed cloud base, with the highest reflectances representing the lowest cloud base, 6 km, and the lowest reflectances representing the highest cloud base, 9 km. For example, the reflectance for 0.664 μm changes from 0.35 for a cloud base of 9 km to 0.59 for a cloud base of 6 km at 178.6°. The near-infrared reflectances did not change as much, from 0.13 to 0.14 for a wavelength of 2.142 μm. This occurs because lower wavelengths are more sensitive to the optical depth (which changes

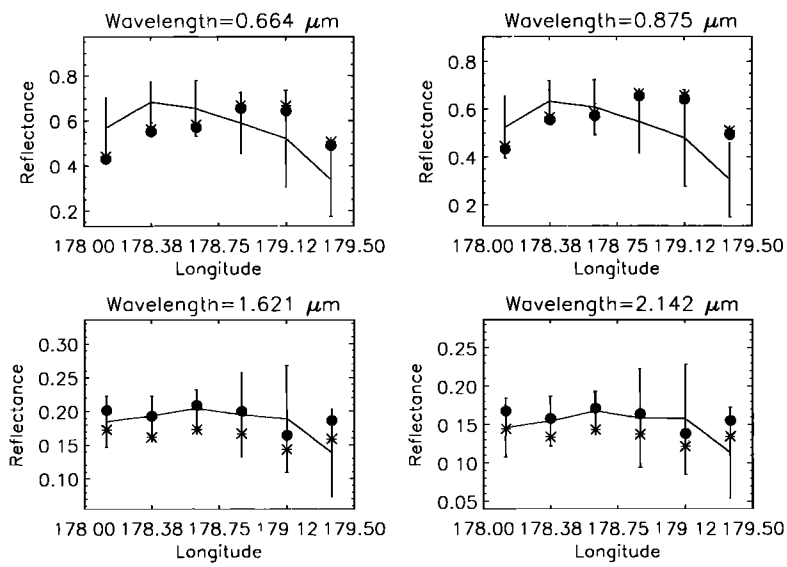

Figure 9. Observed and simulated reflectance, calculated using Monte Carlo radiative transfer code, at the top of the atmosphere as a function of longitude for solar and near-infrared wavelengths. Asteriks represent calculations based on Macke ray-tracing (solid circles), anomalous diffraction theory. Vertical bars represent standard deviations of observed reflectances measured by MODIS Airborne Simulator (MAS), and straight line connects the median radiances.

Table 6. List of Sensitivity Studies Performed to Examine the Effects of Varying Cloud Base, Particle Size, and Particle Shape on the Calculated Top of the Atmosphere Reflectance.

Series	Sensitivity Investigated	Simulation
1	radiative transfer technique	a, Macke ray tracing b, anomalous diffraction theory
2	height dependence of measurements	a, cloud base at 7 km cloud measurements centered at Lear jet altitude b, cloud base at 8 km c, cloud base at 9 km d, cloud base at 6 km e, cloud measurements represent cloud level above f, cloud measurements represent cloud level below
3	assumed shape of small crystals	a, quasi-spheres and Mie scattering b, small crystals are columns c, small crystals are bullet rosettes d, small crystals are polycrystals
4	varying numbers of small crystals	a, MH97 parameterization b, small crystals set to zero c, MH97 multiplied by 2 d, MH97 multiplied by 5 e, MH97 multiplied by 10
5	assumed shape of all ice crystals	a, as measured b, all crystal columns c, all crystal bullet rosettes d, all crystal polycrystals
6	habit classification scheme	a, neural net classification b, Discriminator analysis c, Original classification scheme

with cloud base), whereas the near-infrared channels are more sensitive to particle shape and size near cloud top and are unaffected by changes near cloud base for these optically thick clouds. This dependence on cloud base shows that the need for vertical profiles throughout the whole cloud with colocated radiance measurements.

In series 3, the shapes of crystals with maximum dimensions smaller than 90 μm were varied. Figure 11 shows the calculated reflectances assuming that all small crystals are spheres (S), columns (C), bullet rosettes (B), and polycrystals (P). When small crystals were assumed to be polycrystals, columns, or bullet rosettes

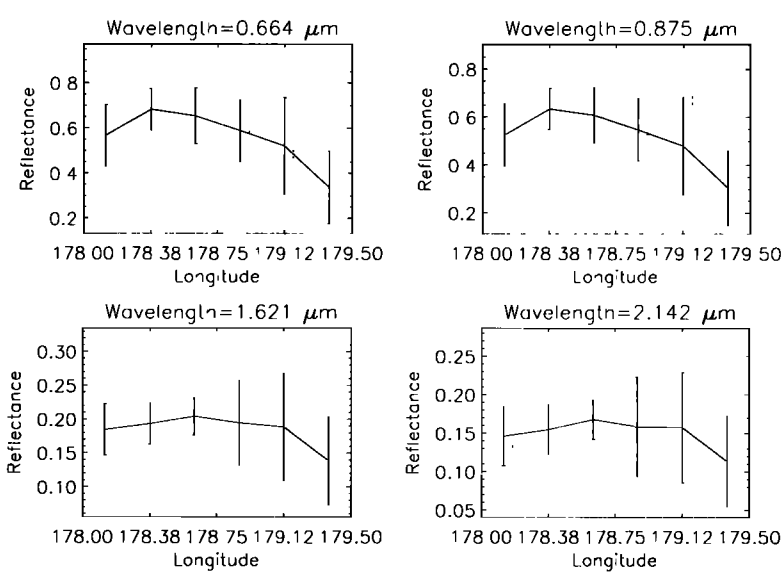

Figure 10. As in Figure 9, observed and simulated reflectances at top of atmosphere. Solid lines represent MAS measurements. Dashed lines represent variation in simulated reflectance depending on the assumed base of the cloud.

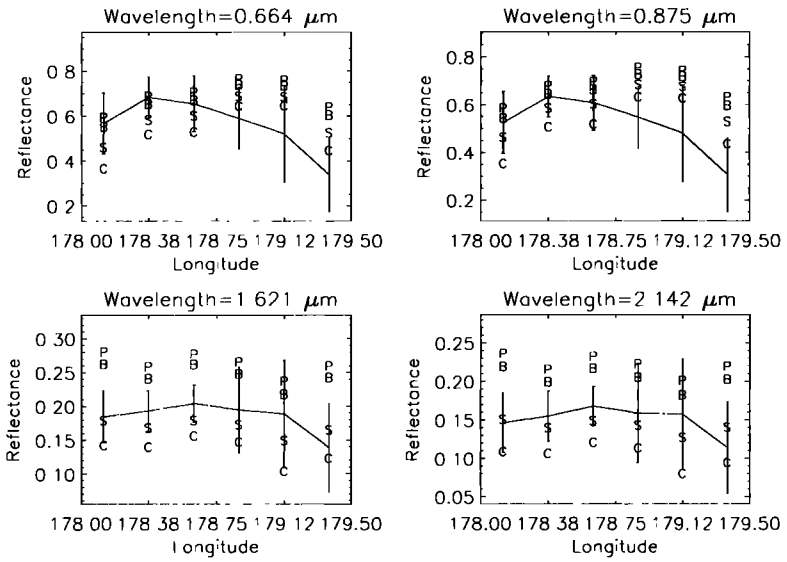

Figure 11. As in Figure 10, solid lines represent MAS measurements. Different letters represent calculated reflectances by varying the shapes of particles smaller than 90 μm: B represents bullet rosettes; P polycrystals, C columns, and S spheres or quasi-spheres.

(instead of quasi-spheres), the 0.664 μm reflectances at 178.6° longitude changed from 0.58 to 0.68, 0.51, or 0.65, respectively. At 2.142 μm, the reflectances changed from 0.14 to 0.23, 0.12, and 0.21, respectively. Some of these changes, especially the low reflectances for the assumed columnar shape, are due to the change in cross-sectional area (and hence extinction optical depth) which occurs when a different shape is assigned to a non varying size distribution. This effect is mixed in with changes in the phase function and single-scattering albedo.

The assumption of varying optical depth differs somewhat from the conventional approach of investigating the effect of shapes, whereby the extinction optical depth is held constant and only the phase function varies for the different shapes. However, given that the size distribution only is obtained from the parameterization and not the shape, the most logical approach was to change both extinction and phase function. Note that even though a parameterization and not direct measurements from the VIPS were used to deduce the small crystal size distribution, the information collected in situ about the shapes of cloud particles (MH96 Figures 22 and 23) is incorporated into this analysis. Since MH97 noted that the cross-sectional area derived from the VIPS-measured particles differed by only 4% from that of circular particles with the same maximum dimension, the assumptions of quasi-spheres is the most realistic for predicting the cloud radiative properties. These sensitivity studies do show that the assumed shapes of the small crystals can significantly affect the predicted cloud radiances, and hence knowledge about typical particle shapes supplied by the VIPS is needed for an accurate prediction of reflectance. It also shows that the radiative properties of quasi-circular small crystals are not adequately predicted by the compact polycrystals; spheres may be a better representation. In an earlier study, *Descloitres et al.* [1998] had shown that polycrystals gave better agreement than did the standard water droplet model to bidirectional reflectances obtained with Polarization and Directionality of Earth Reflectances (POLDER) observations. Some caution must be used in the interpretation of the results as the region of the phase function being sampled (150° to 160°) lies away from the peak between 130° and 140° which is caused by smaller spherical particles (Figure 8), and hence definite conclusions cannot be made.

In series 4, the effects of varying the numbers of small crystals were investigated. Figure 12 shows the calculated reflectances assuming that the number of small crystals is multiplied by 0, 2, 5, or 10 times the number calculated from the MH97 parameterization. The assumed numbers of small crystals can significantly affect the calculated radiance, especially for the visible wavelengths, but also for the near infrared. This is an important consideration, because many previous studies investigating cloud radiative properties used only data from optical array probes, which are unable to adequately estimate the numbers of crystals smaller than 100 μm with the high air speeds involved in the CEPEX study [*Hobbs et al.*, 1996] and hence may not have adequately considered the populations of smaller crystals. The increase in reflectance when the small population is increased by 10 times compared to 5 times is not nearly as large as the increases from zero to 1 time, or 1 to 2 times. This occurs because of the non linear relation between reflectance and extinction optical depth that was previously noted by *Heymsfield et al.* [1998] and others in a broadband perspective.

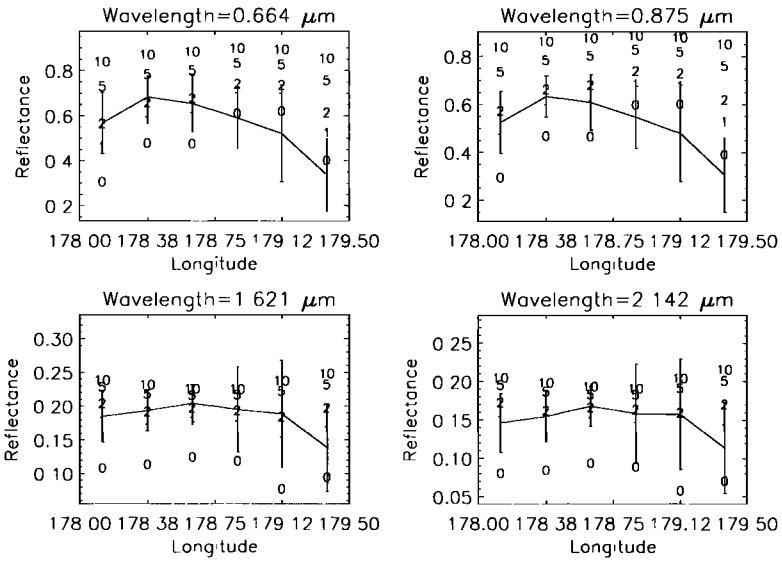

Figure 12. As in Figure 11 except numbers represent factor by which the small crystal contributions were multiplied.

In series 5, the shapes of both large and small ice crystals were varied, while the extinction optical depths were held constant. Because the optical array probes directly measure cross-sectional area, which is proportional to extinction optical depth, this is a quantity known with reasonable accuracy except for the crystals smaller than 90 μm. Only the scattering phase function and single-scattering albedo were varied between simulations. Figure 13 shows the calculated reflectance for the base case (0), and for calculations assuming that all crystals are bullet rosettes (B), polycrystals (P), and columns (C). The reflectances increase for columns, bullet rosettes, and polycrystals in that order. The range of values are similar to those depicted in Figure 11, showing that knowledge of small crystal shapes undetected by optical array probes are as important as the assumptions about larger crystal shapes. For example, at 0.664 μm and 178.6° longitude, the (P), (B), and (C) reflectances of 0.68, 0.65, and 0.51 in Figure 11 changed to 0.73, 0.65, and 0.51, respectively, in Figure 13. At 2.142 μm, the (P), (B), and (C) reflectances change from 0.23, 0.21, and 0.12 in Figure 11 to 0.21, 0.17, and 0.11 respectively, in Figure 13.

The final sensitivity study, series 6, investigated the importance of the habit classification scheme used to identify ice crystal shape. Three different habit classi-

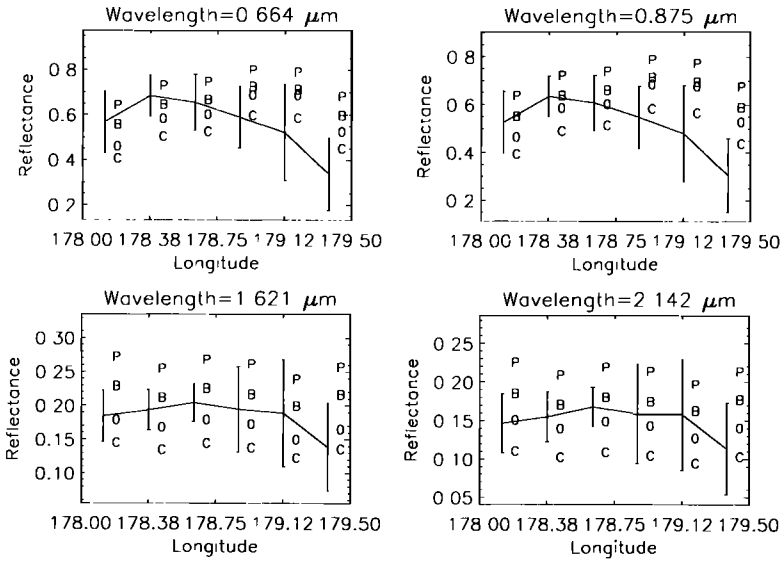

Figure 13. As in Figure 12 except letters represent the shapes of all sizes of ice crystals: 0 indicates base case, P all crystals are polycrystals; B, bullet rosettes; and C, columns.

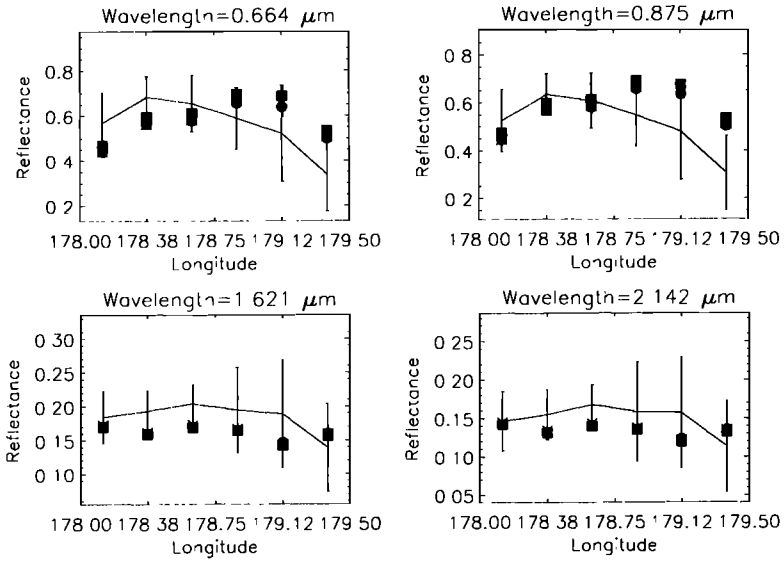

Figure 14. As in Figure 10 except different symbols represent reflectances calculated using different habit classification schemes: solid circles, represent neural-network classification scheme; solid squares, discriminator analysis; and asteriks, original habit classification scheme.

fication schemes were derived in section 3. For all simulations it is assumed that the crystals smaller than 90 μm are quasi-spheres, with scattering properties predicted by Mie theory. The larger crystals have their shapes assigned according to the classification scheme, and minor differences between extinction optical depths exist between cases due to minor differences in the calculated extinction cross sections. Figure 14 shows that the differences in the habit classifications do not significantly affect the calculated reflectances. The only noticeable differences occur in the visible wavelengths, where the discriminator habit scheme (reflectances depicted by solid squares) differs somewhat from the new (solid circles) and original (asteriks hidden by the circles) habit classification schemes. This suggests that assigning correct idealized shapes to the habits is more important than the details of any reasonable classification scheme of assigning the observed crystals to different habits.

5. Conclusions

Using measurements of the sizes and shapes of all sizes of ice crystals acquired on April 4, 1993, during CEPEX, simulated radiances have been computed at multiple solar and near-infrared wavelengths using realistic high-resolution models of ice crystal scattering and Monte Carlo radiative transfer. Although time evolution and a lack of knowledge of cloud base prohibit a highly precise comparison of these simulations with reflectances observed by the MAS, sensitivity studies provide important information about the role of different sizes and shapes of ice crystals in affecting the calculated reflectance. This has important ramifications for remote sensing studies because it offers additional insight for interpreting the measurements of remote sensors. The most important conclusions of the study may be summarized as follows:

1. Crystals smaller than 90 μm, as represented by *McFarquhar and Heymsfield's* [1997] parameterization, dominate the number concentrations and contribute 56% to the total extinction. For the April 4 case, the observed shapes of these crystals and the radiative transfer calculations suggest that the polycrystal model is inadequate for describing smaller ice crystals.

2. "Polycrystals" contribute most, 53%, to the extinction coefficient that is associated with crystals larger than 90 μm. Columns provide 18% and bullet rosettes 29% to the extinction coefficient. Polycrystals here is somewhat of a generic term, where the crystals identified as polycrystals may not be true Koch fractals but could include spatial crystals, aggregates, and other irregular crystals. The simulated reflectances are sensitive to the assumed shapes of the larger crystals.

3. When information about the sizes and shapes of small crystals are incorporated into the calculation of extinction coefficient and mean single-scattering properties, reasonable agreement of the multispectral reflectances at 0.664, 0.875, 1.621, and 2.142 μm calculated with a Monte Carlo radiative transfer code with those observed by the MODIS airborne simulator (MAS) is obtained. Knowledge of the numbers and shapes of small crystals is needed to accurately simulate observed reflectances because the simulated reflectances are very sensitive to these parameters.

4. Some details of the habit classification scheme do not significantly impact the model-predicted reflectances. However, there is evidence that the choice of idealized

crystal shapes used in the habit classification scheme may be more important.

5. The mean-scattering phase function for a distribution of particles, obtained by weighting the scattering phase functions for individual shapes and sizes by the scattering cross sections, are very smooth compared to the individual scattering phase functions. The resolution used for computing these averaged size distributions was much finer than that used in previous studies.

The ambiguity between anomalous diffraction theory and ray tracing and the difficulty in comparing observed radiances with those simulated are not surprising because the observations were based on a complex situation, namely a deep convective layer. Future studies [e.g., *Francis et al.*, this issue] should concentrate on less complex, less thick, slowly evolving cirrus, such as semi transparent homogeneous cirrus over the ocean associated with synoptic uplifting. Nevertheless, the simulations presented here have important climatic implications in that one of the best horizontal and vertical profiles obtained with a tropical anvil has been used to identify the most important factors affecting multispectral reflectances (e.g., crystals smaller than 50 μm can contribute up to 50% of the extinction coefficient) and hence cloud top albedos. For remote sensing, this study implies that multispectral reflectances can be predicted if cloud properties are well known, but the sensitivity studies have shown that without a priori knowledge of ice crystal shapes, it is difficult to precisely solve the inverse problem to predict ice crystal sizes; additional information about ice cloud properties (e.g., geographic location, total optical depth, cloud type) may be needed to convert multispectral reflectances into bulk microphysical parameters. Further, using observed concentrations of small crystals, it has been clearly shown that these sizes affect the observed reflectance. The knowledge gained from these sensitivity studies may help develop algorithms for satellites such as MODIS.

Only four crystal shapes were considered during this study and observed crystal images can show substantial variability from these idealized crystal shapes. More realistic phase functions and representations of ice crystals are crucial for performing these radiative transfer codes. In addition, instantaneous vertical profiles throughout a cloud would be very beneficial so that simulated reflectances could be compared against observed reflectances to test the adequacy of the assumed particle shapes.

Acknowledgments. The support of the NSF Climate Dynamics Program, NSF award ATM-9640613, the Center for Clouds, Chemistry and Climate (C^4) at the Scripps Institution of Oceanography, and by the NASA EOS program is acknowledged. The efforts of the Aeromet Lear jet crew (R. Hobbs, D. Rusk, R. Wallin, and B. Jones) to obtain the high-quality microphysical measurements are appreciated. The comments of A. Baran, X. Wu, and an anonymous reviewer were appreciated. The National Center for Atmospheric Research (NCAR) is sponsored by the National Science Foundation.

References

Arnott, W.P., Y. Dong, J. Hallett, and M.R. Poellot, Role of small ice crystals in radiative properties of cirrus: A case study, FIRE II, 22 November 1991, *J. Geophys. Res., 99*, 1371-1381, 1994

Auer, A., and D. Veal, The dimensions of ice crystals in natural clouds, *J. Atmos. Sci., 27*, 919-926, 1970.

Descloitres, J., J.C. Buriez, F. Parol, and Y. Fouquart, POLDER observations of cloud bidirectional reflectances compared to a plane-parallel model using the International Satellite Cloud Climatology Project cloud phase functions, *J. Geophys. Res., 103*, 11411-11418, 1998

Francis, P.N., J.S. Foot, and A.J. Baran, Aircraft measurements of the solar and infrared radiative properties of cirrus and their dependence on ice crystal shape, *J. Geophys. Res.*, this issue.

Fu., Q., An accurate parameterization of the solar radiative properties of cirrus clouds for climate models, *J. Clim., 9*, 2058-2082, 1996.

Heymsfield, A.J., Ice crystal terminal velocities, *J. Atmos. Sci., 29*, 1348-1357, 1972.

Heymsfield, A.J., Cirrus uncinus generating cells, 269 pp., Ph.D. thesis, Univ. of Chicago, Ill., 1973.

Heymsfield, A.J., and G.M. McFarquhar, On the high albedos of anvil cirrus in the tropical Pacific warm pool: Microphysical interpretations from CEPEX and Kwajalein, Marshall Islands, *J. Atmos. Sci., 53*, 2424-2451, 1996.

Heymsfield, A.J., G.M. McFarquhar, W.D. Collins, J.A. Goldstein, F.P.J. Valero, J. Spinhirne, W. Hart, and P. Pilewskie, Cloud properties leading to highly reflective tropical cirrus: Interpretations from CEPEX, TOGA COARE, and Kwajalein, Marshall Islands, *J. Geophys. Res., 103*, 8805-8812, 1998.

Hobbs, R., B. Morrison, R. Ashenden, and R.F. Ide, Comparison of two data processing techniques for optical array probes, paper presented at International Conference on Aircraft Inflight Icing, FAA, Springfield, Va., 1996.

Iaquinta, J., H. Isaka, and P. Personne, Scattering phase function of bullet rosette ice crystals, *J. Atmos. Sci., 52*, 1401-1413, 1995.

Jayaweera, K.O.L.F., and B.J. Mason, The falling motions of loaded cylinders and discs simulating snow crystals, *J. Fluid. Mech., 22*, 151-156, 1965.

King, M.D., and others, Airborne scanning spectrometer for remote sensing of cloud, aerosol, water vapor, and surface properties, *J. Atmos. Oceanic. Technol., 13*, 777-794, 1996.

Kinne, S., and K.-N. Liou, The effects of the nonsphericity and size distribution of ice crystals on the radiative properties of cirrus clouds, *Atmos. Res., 24*, 273-284, 1989.

Kinne, S., T.P. Ackerman, A.J. Heymsfield, F.P.J. Valero, K. Sassen, and J.D. Spinhirne, Cirrus microphysics and radiative transfer: Cloud field study on 28 October 1986, *Mon. Weather Rev., 120*, 661-684, 1992.

Kohonen, *Self-organizing maps*, in *Springer Series in Information Sciences*, 362 pp., Springer-Verlag, New York, 1995.

Kou, L., D. Labrie, and P. Chylek, Refractive indices of water and ice in the 0.65- to 2.5 micron spectral range, *Appl. Opt., 32*, 3531-3540, 1994.

Krupp, C., Holographic measurements of ice crystals in cirrus clouds during the International Cirrus Experiment ICE 1989, in *Report of the Fourth ICE Workshop* Meteorol. Off. College, edited by R.W. Saunders and P.R.A. Brown, Reading, England, 1991.

Lilly, D.K., Cirrus outflow dynamics, *J. Atmos. Sci., 45*, 1594-1605, 1988.

Macke, A., Scattering of light by polyhedral ice crystals, *Appl. Opt., 32*, 2780-2788, 1993.

Macke, A., J. Mueller, and E. Raschke, Single scattering properties of atmospheric ice crystals, *J. Atmos. Sci.*, *53*, 2813-2825, 1996.

Macke, A., P.N. Francis, G.M. McFarquhar, and S. Kinne, The role of ice particle size distributions in cirrus cloud radiative transfer, *J. Atmos. Sci.*, *55*, 2874-2883, 1998.

McFarquhar, G.M., and A.J. Heymsfield, Microphysical characteristics of three cirrus anvils sampled during the Central Equatorial Pacific Experiment, *J. Atmos. Sci.*, *53*, 2401-2423, 1996.

McFarquhar, G.M., and A.J. Heymsfield, Parameterization of tropical cirrus ice crystal size distributions and implications for radiative transfer: Results from CEPEX, *J. Atmos. Sci.*, *54*, 2187-2200, 1997.

Miloshevich, L.M., A.J. Heymsfield, and P.M. Norris, Microphysical measurements in cirrus clouds from ice crystal replicator sondes launched during FIRE II, *Proc. 11th Int. Conf. Clouds and Precip.*, 525-528, 1992.

Mishchenko, M.I., D.J. Wielaard, and B.E. Carlson, T-matrix computations of zenith-enhanced lidar backscatter from horizontally oriented plates, *Geophys. Res. Lett.*, *24*, 771-774, 1997.

Mitchell, D.L., and W.P. Arnott, A model predicting the evolution of ice particle size spectra and radiative properties of cirrus clouds. II, Dependence of absorption and extinction on ice crystal morphology, *J. Atmos. Sci.*, *51*, 817-832, 1994.

Muinonen, K., T. Nousiainen, P. Fast, K. Lumme, and J.I. Peltoniemi, Light scattering by Gaussian random particles: Ray optics approximation, *J. Quant. Spectr. Radiat. Transfer*, *55*, 577-601, 1996.

Perovich, D., and J. Govoni, Absorption coefficients of ice from 250 to 400 nm, *Geophys. Res. Lett.*, *18*, 1233-1235, 1991.

Spinhirne, J.D., W.D. Hart, and D.L. Hlavka, Cirrus infrared parameters and shortwave reflectance relations from observations, *J. Atmos. Sci.*, *53*, 1438-1458, 1996.

Takano, Y., and K. Jayaweera, Scattering phase matrix for hexagonal ice crystals computed from ray optics, *Appl. Opt.*, *24*, 3254-3263, 1985.

Warren, S., Optical constants of ice from the ultraviolet to the microwave, *Appl. Opt.*, *23*, 1206-1225, 1984.

S.M. Aulenbach, A.J. Heymsfield, G.M. McFarquhar, National Center for Atmospheric Research, P.O. Box 3000, Boulder, CO 80307-3000. (e-mail: mcfarq@ncar.ucar.edu)

J. Iaquinta, Ussel, France (e-mail: jean.iaquinta@wanadoo.fr)

A. Macke, Institut fuer Meereskunde, Abt. Maritime Meteorologie, Duesternbrooker Weg 20, 24105 Kiel, Germany (e-mail: amacke@ifm.uni-kiel.de)

(Received December 21, 1998; revised July 23, 1999; accepted July 27, 1999.)